Bulletin of the Seismological Society of America, Vol. 81, No. 4, pp. 1129–1144, August 1991

COMPLEX FAULTING DEDUCED FROM BROADBAND MODELING OF THE 28 FEBRUARY 1990 UPLAND EARTHQUAKE (M_L = 5.2)

BY DOUGLAS S. DREGER AND DONALD V. HELMBERGER

ABSTRACT

The 1990 Upland earthquake was one of the first sizable local events to be recorded broadband at Pasadena, where the Green's functions appropriate for the path are known from a previous study. The synthetics developed in modeling the 1988 Upland sequence were available for use in rapid assessment of the activity. First-motion studies from the Caltech-USGS array data gave two solutions for the 1990 main shock based on the choice of regional velocity models. Although these focal mechanisms differ by less than 5° in strike and 20° rake, it proved possible to further constrain the solution using these derived Green's functions and a three-component waveform inversion scheme. We obtain from long-period waves a fault-plane solution of $\theta = 216°$, $\delta = 77°$, $\lambda = 5.0°$, $M_0 = 2.5 \times 10^{24}$ dyne-cm, depth = 6 km, and a source duration of 1.2 sec, for which the orientation and source depth are in good agreement with the first-motion results of Hauksson and Jones (1991). Comparisons of the broadband displacement records with the high-pass Wood–Anderson simulations suggests the 1990 earthquake was a complicated event with a strong asperity at depth. Double point-source models indicate that about 30 per cent of the moment was released from a 9-km deep asperity following the initial source by 0.0 to 0.5 sec. Our best-fitting distributed fault model indicates that the timing of our point-source results is feasible assuming a reasonable rupture velocity. The rupture initiated at a depth of about 6 km and propagated downward on a 3.5 by 3.5 km (length by width) fault. Both the inversion of long-period waves and the distributed fault modeling indicate that the main shock did not rupture the entire depth extent of the fault defined by the aftershock zone. A relatively small asperity (about 1.0 km^2) with a greater than 1 kbar stress drop controls the short-period Wood–Anderson waveforms. This asperity appears to be located in a region where seismicity shows a bend in the fault plane.

INTRODUCTION

The occurrence of the Upland, California, M_L = 5.2 earthquake on 28 February 1990, approximately 43 km east of the IRIS/TERRAscope broadband, high-dynamic range station at Pasadena, California (PAS), provided an opportunity to compare waveforms of different sized events from the same source region. In particular, the waveforms of the 1990 main shock are compared with those of two smaller events that occurred on 26 June and 6 July 1988. Such comparisons prove to be very fruitful in studying source complexities of larger earthquakes. The high-dynamic range of the PAS station allows one to study the smaller, more frequent events as well as the larger events. Using the waveforms of smaller earthquakes with relatively simple sources allows the effects of the propagation path on the waveforms to be identified. The broadband character of the seismograms allows many distinct phases with different frequency content to be studied together in a whole waveform modeling exercise.

Records of the 26 June 1988 (M_L = 4.6) Upland event and its largest aftershock (M_L = 3.7 on 6 July 1988) were used in an earlier study (Dreger and Helmberger, 1990) to examine the effects of various crustal structure models on wave propagation. In that study, one-dimensional and two-dimensional velocity models were tested for the path from Upland to PAS. Gradient structures, deep crustal-velocity structure, and near-receiver two-dimensional structures were evaluated in terms of the effect on the synthetic waveforms. The results of that study indicate that a one-dimensional layer over a half-space model works very well in producing synthetic seismograms which accurately model the data. The preferred plane layered model was LOHS1 (Table 1). The source depths of the 1988 M_L = 4.6 and M_L = 3.7 events were determined to be 6 km and 9 km, respectively.

Figure 1 shows the location of PAS, together with the locations of the two 1988 Upland events and the 1990 main shock as calculated by the Caltech-USGS, Southern California Seismic Network (SCSN). These events occurred in nearly the same location and share similar propagation paths. PAS is located at a distance of about 43 km at an azimuth of about 272° from the 1990 main shock epicenter. The four focal mechanisms shown on Figure 1 were determined from SCSN first-motion polarities. Mechanisms M1 and M2 were determined for the 26 June and 6 July 1988 Upland events, respectively. Mechanisms M3 and M4 were computed for the 1990 main shock. A number of researchers computed these focal mechanisms, and the focal mechanism parameters and references are listed in Table 2. The effects of the focal mechanisms M1 and M2 on synthetics computed using model LOHS1 are discussed in Dreger and Helmberger (1990). The focal mechanism M3 was determined by Hauksson and Jones (1991) for the 1990 main shock using a regional one-dimensional velocity model (SoCal, Table 1). They used a different velocity model with slower near-surface velocities for stations located in Los Angeles basin. Focal mechanism M4 was calculated for the 1990 main shock using a three-dimensional velocity model (H. Magistrale, personal comm., 1990). All of these focal mechanisms are very similar. Of the two possible fault planes, the southwest-trending plane is favored for the 1988 main shock based on observed directivity (Mori and Hartzell, 1990). The locations of the 1990 aftershocks (Fig. 2a) show that these events also occurred on a southwest-trending fault plane where the depths of the aftershocks (Fig. 2b) range from about 3 to 13 km on a northwest-dipping plane (Hauksson and Jones, 1991). The southwest-trending fault plane has a

TABLE 1

ONE-DIMENSIONAL VELOCITY MODELS

LOHS1				SoCal			
V_p	V_s	ρ	Z	V_p	V_s	ρ	Z
4.5	2.6	2.4	0.0	5.5	3.18	2.4	0.0
5.9	3.5	2.67	4.0	6.3	3.64	2.67	5.5
6.6	3.8	2.8	16.0	6.7	3.87	2.8	16.0
8.0	4.1	3.1	26.0	7.8	4.5	3.0	37.0
8.2	4.2	3.3	30.0				

V_p is the compressional-wave velocity in km/sec; V_s is the shear-wave velocity in km/sec; ρ is the density in g/cm^3; and Z is the depth to the top of the layer in km.

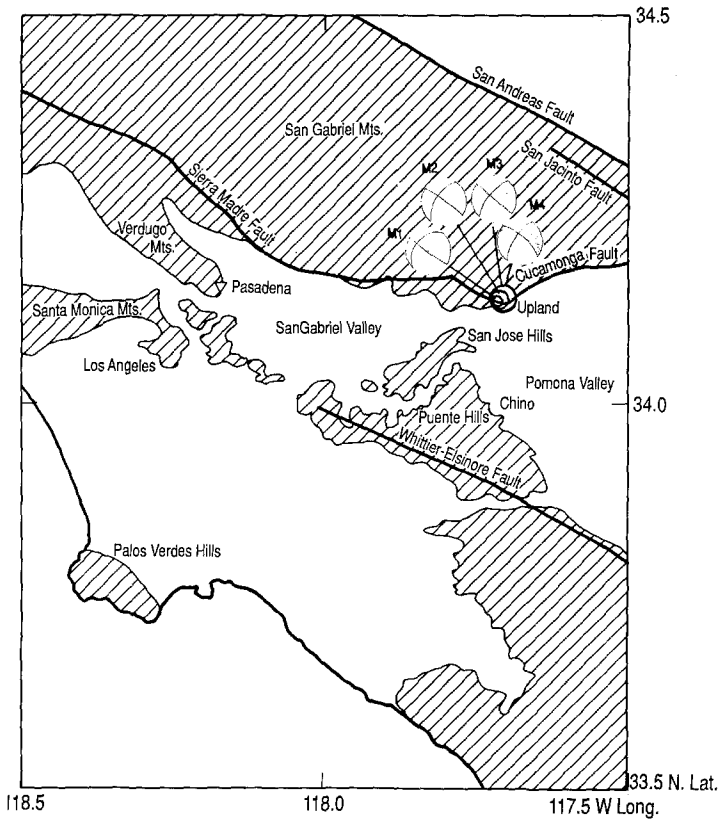

FIG. 1. Location map: the inverted triangle is the Pasadena station and the circles denote the Upland events, scaled to magnitude. Focal mechanisms M1 and M2 are for the 1988 main shock and aftershock, respectively; M3 and M4 are for the 1990 main shock. All focal mechanisms were determined from first-motion polarities on the Caltech/USGS seismic array. Hatched regions represent areas of shallow or surficial basement rocks after Yerkes *et al.* (1965).

TABLE 2

FIRST-MOTION POLARITY FOCAL MECHANISMS

ID	Strike (°)	Dip (°)	Rake (°)	Reference
M1	221	40	8	L. Jones (personal comm.)
M2	212	60	−6	L. Jones (personal comm.)
M3	220	70	0	Hauksson and Jones (1991)
M4	215	70	−20	H. Magistrale (personal comm.)

left lateral sense of motion, which is consistent with the inferred motion of the Cucamonga fault in this area (Cramer and Harrington, 1987). Fault-plane solutions for the 1988 aftershock and the 1990 main shock (Table 2) have steep dips for the southwest-trending plane that are consistent with the observed aftershock distribution for the 1990 sequence.

The aim of this study is to utilize the Green's functions developed in the earlier work to determine the source characteristics of the 28 February 1990 Upland, California, main shock, using the broadband data recorded at PAS. We use a frequency-wavenumber (F-K) approach (Saikia, manuscript in

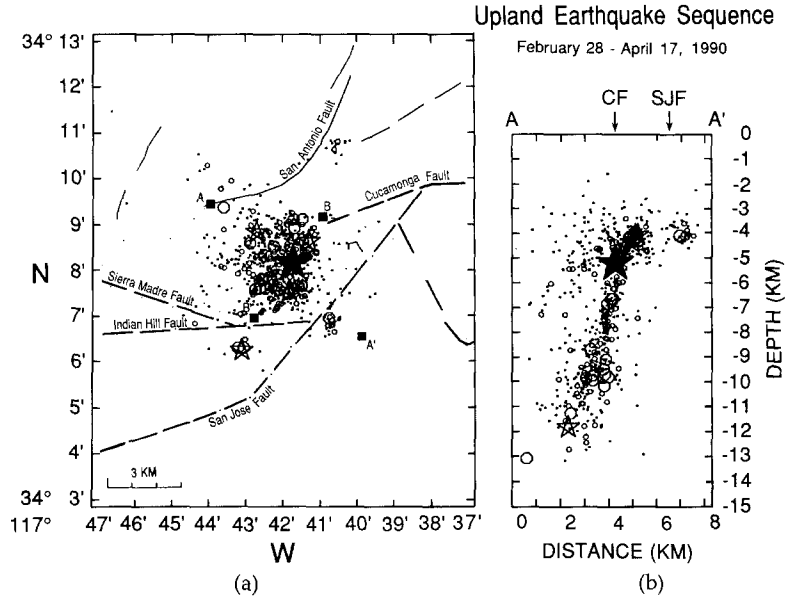

FIG. 2. (a) Map view and (b) depth section locations of the 28 February 1990 Upland sequence (modified from Hauksson and Jones, 1991). The main shock is denoted by the solid star. AA′ shows the location of the depth section. BB′ shows the location of the top (depth of 6 km) of the fault we used in the distributed fault calculations shown in Figure 7.

preparation) to compute synthetic seismograms. This approach computes the complete solutions for a layered stack, including near-field terms. All of the synthetics in this article were computed using the LOHS1 velocity model (Table 1). We use these synthetics to invert for long-period source parameters (orientation, moment, depth, time function) and to model the data using point-source and finite distributed source models.

DATA COMPARISONS AND ANALYSIS

As stated above, the 1990 sequence occurred in about the same location and had a focal mechanism similar to the two largest events of the 1988 sequence. Since location and orientation are nearly the same, there should be similarities in the waveforms of these three events. Figure 3 displays the displacement data and short-period Wood–Anderson (WASP) convolutions for the 1990 main shock, 1988 main shock, and 1988 aftershock. To the first order, similarities in the waveforms are readily apparent. On the tangential component the direct S (S_0), multiple S (S_1), and Love waves are all observed. Beginning at the P-wave travel time, there is a ramp shaped phase that continues to the phase S_0. This phase was identified as a near-field arrival (Dreger and Helmberger, 1990). The three events are also similar in that the tangential components have the largest displacement amplitudes followed by the radial and then the vertical components. The displacement records for the 1990 main shock and the 1988 main shock are the most similar. Both events have approximately the same S_0 to S_1 ratio, and the amplitude ratios of the Love wave to S_0 and S_1 are also nearly the same. In addition, the long-period coda is also well correlated. The largest difference between these two events is that the 1990 main shock has a larger long-period to short-period energy ratio compared to the 1988 main shock, due to a relatively larger fault area. A curious observation for the 1990 main shock,

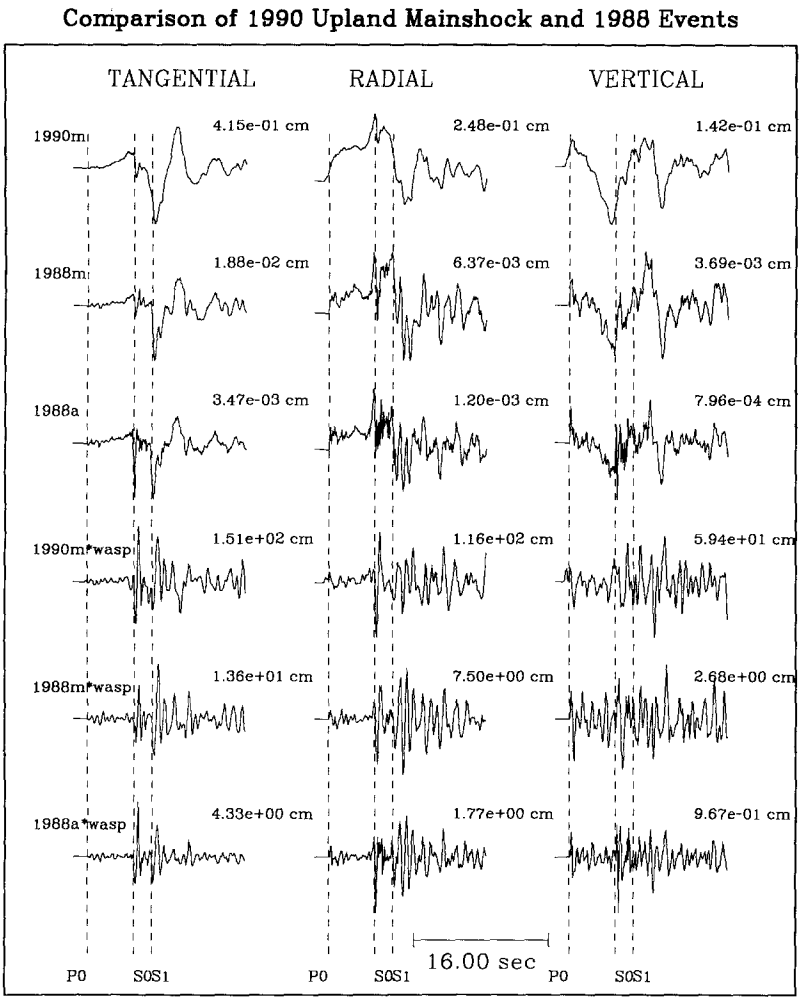

FIG. 3. Three-component displacement data for the 28 February 1990 (1990m), 26 June 1988 (1988m), and 6 July 1988 (1988a) Upland earthquakes. 1990m*wasp, 1988m*wasp, and 1988a*wasp are the respective displacements convolved with the short-period Wood-Anderson (WASP) instrument response. The labels P_0, S_0, and S_1 mark the arrival times of direct P, direct S, and multiple S. The amplitudes are in centimeters.

however, is that, while the displacement waveforms generally appear longer period than the 1988 data, the phase S_0 does not. The 1988 main shock was best modeled using a source depth of 6 km (Dreger and Helmberger, 1990). Thus, the similarity in the waveforms suggests that these two events occurred at nearly the same depth, with similar focal mechanisms. The focal depth of the 1990 main shock determined from SCSN first motions was 5.2 km (Hauksson and Jones, 1991), which is in agreement with the first-order depth estimate obtained above by simply comparing the waveforms.

Next we compare the tangential WASP records. The 1990 main shock most closely resembles the WASP record of the 1988 aftershock (depth = 9 km), not that of the 1988 main shock (depth = 6 km). This is in contrast to the displacement records just discussed, suggesting that the short-period energy originated closer to the location of the 1988 aftershock. Considering the effect of source

depth on the phases S_0 and S_1 discussed in Dreger and Helmberger (1990), it appears that the short-period energy originated at a greater depth than the longer period energy, suggesting the existence of an asperity at depth.

If one examines the direct P waves on the radial and vertical component WASP records, there is clearly a double pulse for the 1990 main shock compared to the single pulse observed for both the 1988 main shock and aftershock. This indicates that the 1990 main shock is indeed more complicated than a simple point source with a simple time function. In order to align the tangential data along S_0 and S_1 arrival times, it was necessary to advance the 1990 main shock 0.4 sec. The line showing P_0 is aligned on the first-arrival P waves of the 1988 data. The P_0 line aligns with the second pulse of the P wave for the 1990 main shock. This suggests that a second source follows the first arrival by about 0.4 sec. On the tangential component there is also a relatively large phase before the line S_0 compared to the 1988 data, which may be due to a complicated source. To address this apparent complexity, we examine double point-source models and distributed fault models.

Point-Source Models

As discussed earlier, the two fault-plane solutions determined from first-motion polarities and the depth distribution of aftershocks for the 1990 main shock indicate that this event occurred on a steeply dipping plane. To provide further constraint to the fault-plane orientation and to obtain an estimate of the long-period source-time function and seismic moment, we invert the three-component displacement data convolved with a Press-Ewing instrument response (see Fig. 4). The method we employ is that of Liu and Helmberger (1985), in which the fault-plane parameters (strike(θ), dip(δ), and rake(λ)) are iteratively solved for in a least-squares sense using an amplitude sensitive error function defined as

$$e_i = \int_0^T \left[f_i(t) - g_i(t) \right]^2 dt, \tag{1}$$

where $f_i(t)$ and $g_i(t)$ are the data and synthetic for the ith component and T is the length of the record being inverted. Seismic moment and time function are determined by mapping the error space and determining the combination of parameters that minimizes the error defined by (1). The whole waveform is used in the inversion. A more detailed description of the method and resolution capabilities will be given in Dreger and Helmberger (manuscript in preparation).

Source depths of 4.5, 6, 7, and 8 km were tested and a source depth of 6 km gave the lowest errors. Using this source depth, a best-fitting long-period point-source solution of $\theta = 216°$, $\lambda = 5°$, $\delta = 77°$, $M_0 = 2.5 \times 10^{24}$ dyne-cm, and a source duration (τ) of 1.2 sec was obtained. Helmberger and Malone (1975) define τ as $(0.5\delta T_1 + \delta T_2 + 0.5\delta T_3)$, where the δT's represent the length of the positive, zero, and negative slopes of a trapezoidal time function. For simplicity, we limited the trapezoidal time function to the case where the δT's are all the same value.

Figure 4a compares the data to synthetic waveforms determined by the inversion. The waveforms are in good agreement in both waveshape and amplitude. Figure 4b is a plot showing the error as a function of both moment and τ. The lowest error occurs for a moment of 2.5×10^{24} dyne-cm and a $\tau = 1.2$ sec. The region of lowest error indicates that τ can range from 1.0 to

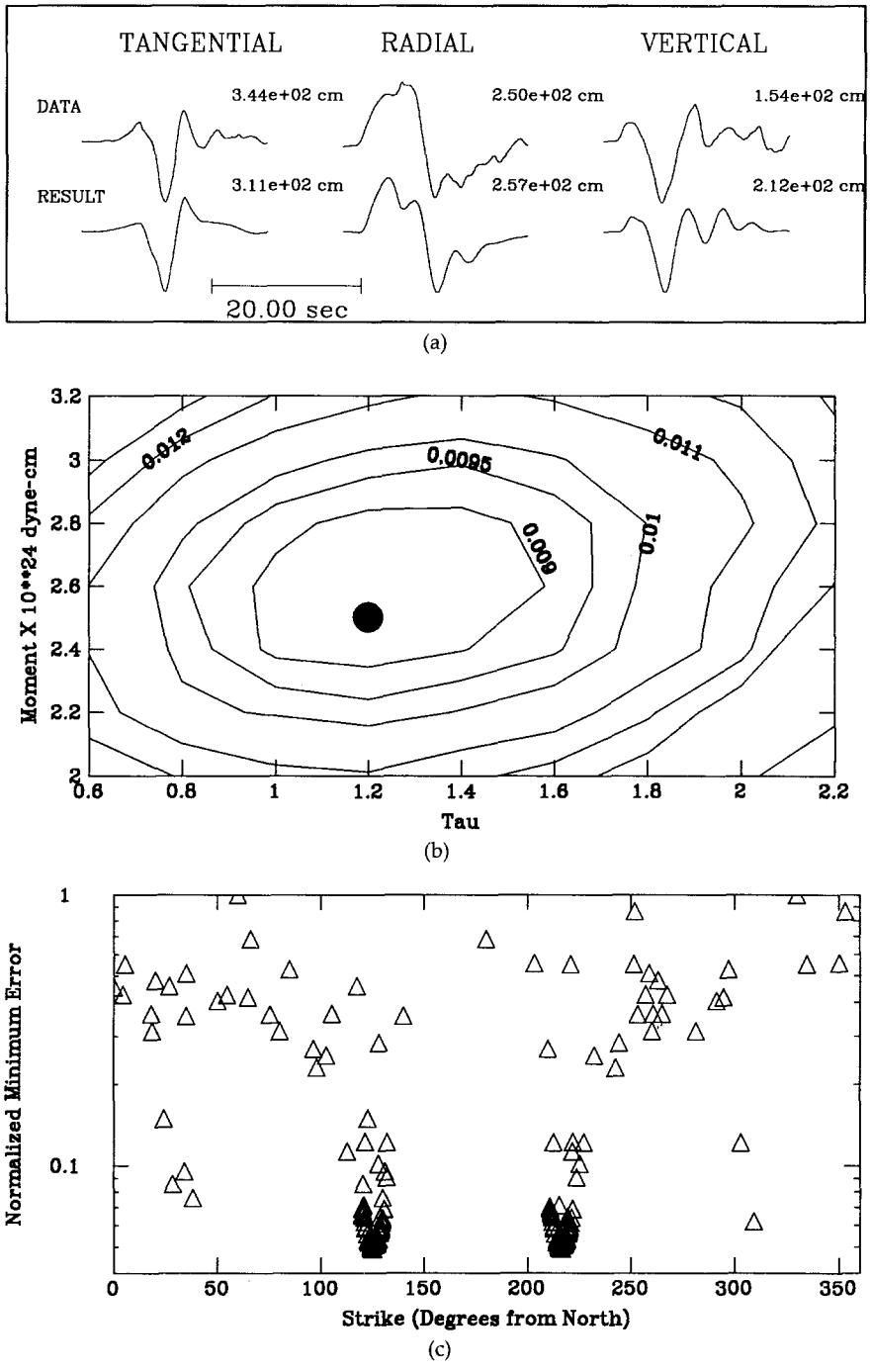

FIG. 4. Long-period inversion results. (a) compares displacement data convolved with the instrument response of a Press-Ewing instrument to synthetics determined by waveform inversion. The amplitudes are in centimeters. (b) Misfit error defined by equation (1) as a function of seismic moment and source duration (τ). The filled circle marks where the lowest misfit error occurs. (c) Normalized minimum error as a function of strike (θ) for the moment and τ indicated by the circle in (b). Each triangle represents the error of a single iteration where both the auxiliary fault plane and the fault-plane solution determined by the inversion are plotted. Four different starting models (starting fault-plane solutions) were used in these calculations. The inversion results are: $\theta = 216°$, $\lambda = 5°$, $\delta = 77°$, and $M_0 = 2.5 \times 10^{24}$ dyne-cm.

about 1.5 sec and moment (2.4–2.8) $\times 10^{24}$ dyne-cm. An alternative definition of duration (τ) for a circular fault, after Brune (1970), is

$$\tau = \frac{2.62\,a}{\beta}, \tag{2}$$

where a is the radius of a circular fault and β is the shear velocity in the vicinity of the source (Cohn *et al.*, 1982). For the above range in τ, the area of faulting for a circular fault is between about 6 to 13 km^2. This is much less than suggested by the aftershock distribution (Figs. 2a and b), for which an area of 40 km^2 is obtained. Figure 4c shows the behavior of the fitting error to the model parameter θ. Similar plots for δ and λ show that the solution is also unique for these parameters.

As discussed in the last section, there is some evidence that the main shock was a relatively complicated event. To address this possibility, several single and double point-source models were considered, as shown in Figure 5. The synthetics were computed using the fault-plane solution and moment obtained above. The top trace shows the 1990 three-component displacement and the tangential WASP data. The first synthetic shown (6km.lng) is for a source depth of 6 km and a long-period trapezoidal time function with $\tau = 1.2$ sec. These synthetics explain the observed durations of S_1 and the Love wave well, but they are depleted in short-period energy as compared to the data. Both the phase S_0 in the tangential displacement data and the tangential WASP waveform are poorly modeled by the long-period source time function. Next we compare synthetics with a source depth of 6 km and a shorter time function (6km.shrt) to the data. For this model, a trapezoidal time function with $\tau = 0.3$ sec is used. Here the phase S_0 on the tangential component is fairly well modeled, but the rest of the synthetic displacement waveforms are generally too short period. The frequency content of the WASP record seems to be correct, although the synthetic waveform is in poor agreement with the data. Next synthetics computed using a source depth of 9 km (9km.shrt) and the short-period time function used above in model 6km.shrt are compared with the data. The displacement synthetics clearly do not fit the displacement data, however the tangential WASP record is well modeled by the 9-km source depth, and the period of the WASP synthetic matches that of the WASP data.

Summarizing, the inversion of the three-component long-period waveforms results in a fault-plane solution that is compatible with that obtained by Hauksson and Jones (1991). The minimum in the waveform fitting error for τ between 1.0 and 1.5 sec shows that an upper bound for the fault area is about 13 km^2, which is much les than is suggested by the aftershock distribution (Figs. 2a and b), indicating that perhaps the main shock did not rupture the entire area of the aftershock zone. For reference, a circular fault with a τ of 2.0 sec yields from equation (2) an area of 22 km^2, which is still only 56 per cent of the area defined by the aftershock zone. Comparison of the displacement data to displacement synthetics computed with the source parameters obtained by the inversion of long-period waves shows that the displacement records, with the exception of the phase S_0, are better modeled by a point source with a source depth of 6 km and a relatively long-period time function ($\tau = 1.2$ sec). The tangential WASP data, however, is better modeled using a point source at 9 km depth and a shorter period time function ($\tau = 0.3$ sec).

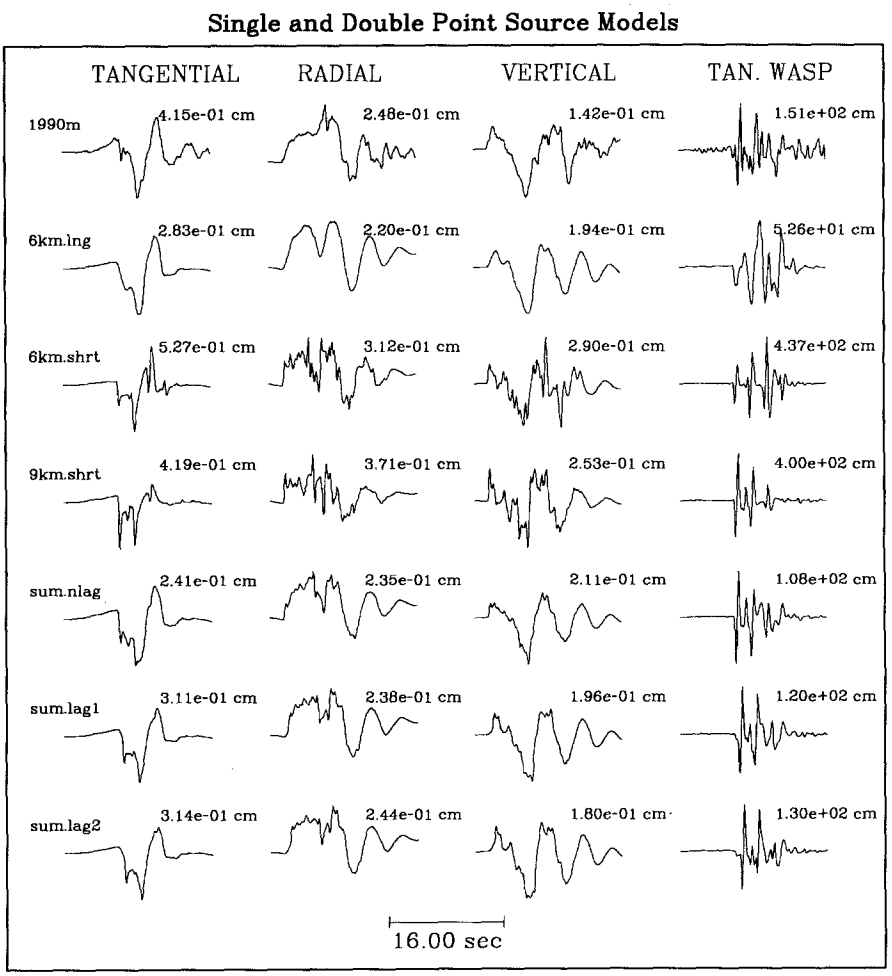

FIG. 5. Three-component displacement and tangential component WASP data for the 28 February 1990 main shock, and single (6km.lng, 6km.shrt, and 9km.shrt) and double point (sum.nlag, sum.lag1, and sum.lag2) source models. Synthetics were computed using an F-K method, and the focal mechanism and seismic moment determined by inversion of the long-period waves (Fig. 4). See text for details of the source-time functions and lag times used. The amplitudes are in centimeters.

To examine the possibility of a double source, we simply added the 6km.lng and 9km.shrt synthetics together with various time lags and amplitude weightings following a trial-and-error procedure. It was found that the deeper source (9km.shrt) with about 30 per cent of the total moment release worked reasonably well. The constraint used was the amplitude ratio of the tangential WASP to the tangential displacement, for which the data has a value of about 360. The long-period point-source model underestimates this value by a factor of about 2, while the short-period point-source synthetics overestimate it by more than a factor of 2. In the following double point-source models, we use the 30 per cent weighting value and demonstrate the effects of shifting the sources in time. The long-period moment estimate obtained earlier is the total moment used in the double point-source models.

The first model (sum.nlag) has no time lag between the two point sources. This model exhibits a reasonable fit to the data. The long duration of S_1 and the

Love wave is maintained, while S_0 is shorter period. The tangential WASP is also well modeled and the WASP to displacement ratio is about 440. The second model (sum.lag1) considers the case where the 9-km-deep source is lagged in time by 0.5 sec. This synthetic fits better than the case with no time lag because of improvements to the shape of direct P (P_0), in which there is a break in slope on the displacement P waveforms as observed in the data. The timing between S_0 and S_1 is also good. In addition, the two distinct S_0 phases observed in the data are beginning to separate in the synthetics and the phase S_0 is distinctly sharper than the phase S_1 and the Love wave. The WASP to displacement ratio is about 370. The third model (sum.lag2) is a summation in which the deeper source is lagged by 0.75 sec. The shape of direct P (P_0) on the radial and vertical components is well modeled as are the three-component displacement records. In addition, the tangential WASP is very well modeled. Two S_0 phases are produced, and the WASP to displacement ratio is about 400. With increasing lag time between the sources however, the separation of S_0 and S_1 becomes too small. This is due to interference of the S_1 phases for the long- and short-period sources. Since the S_0 phase for the long-period source is rather subdued, the addition of the short-period source does not produce the same kind of interference for S_0. The waveforms in Figure 5 demonstrate that simple, single point-source models do not adequately model the data and that a double point-source model better explains both the long- and short-period waveform data. This is similar to the result of Kanamori *et al.* (1990), in which they found that, to explain both the long-period and short-period phases recorded for the 3 December 1988 Pasadena earthquake recorded at PAS, two time functions were needed. In particular, a long-period time function was needed to explain the near-field displacements, but it failed to model the far-field pulses, which required a shorter period time function.

Judging from models sum.nlag and sum.lag1, the time lag of the second deeper source could be between 0.0 and 0.5 sec, although the 0.5 sec value is close to the timeshift used to align the 1990 data in Figure 3. The case where there is no lag time could mean that the deeper, short-period event is not directly related to a propagating rupture front but a subevent more closely akin to an aftershock. The case where there is a lag time could be as above but may also be due to an asperity triggered by a propagating rupture front. The next section examines the second case in more detail.

Before moving on to the distributed fault models, it is interesting to use the double point-source model sum.lag1 in the long-period waveform inversion to see the effect on the orientation and moment estimate. It is assumed that both the long-period and short-period sources have the same orientation. Figure 6 shows the results of this inversion. Visually the fit to the long-period data is as good as in Figure 4a, however there is a slightly larger waveform fitting error. The waveshapes and amplitudes show little change at long periods, and the inversion results in only a slightly different solution where $\theta = 215°$, $\lambda = 6°$, $\delta = 74°$, and $M_0 = 2.5 \times 10^{24}$ dyne-cm. The differences are only a 1° change in strike (θ) and rake (λ) and a 3° change in dip (δ). Comparing the displacements and tangential WASP data to synthetics computed with this solution, however, produces better agreement in maximum amplitudes. Thus, the addition of a second, short-period source doesn't appreciably affect the fault-plane solution obtained by inverting the long-period waves, but it results in better agreement with the displacement and WASP data.

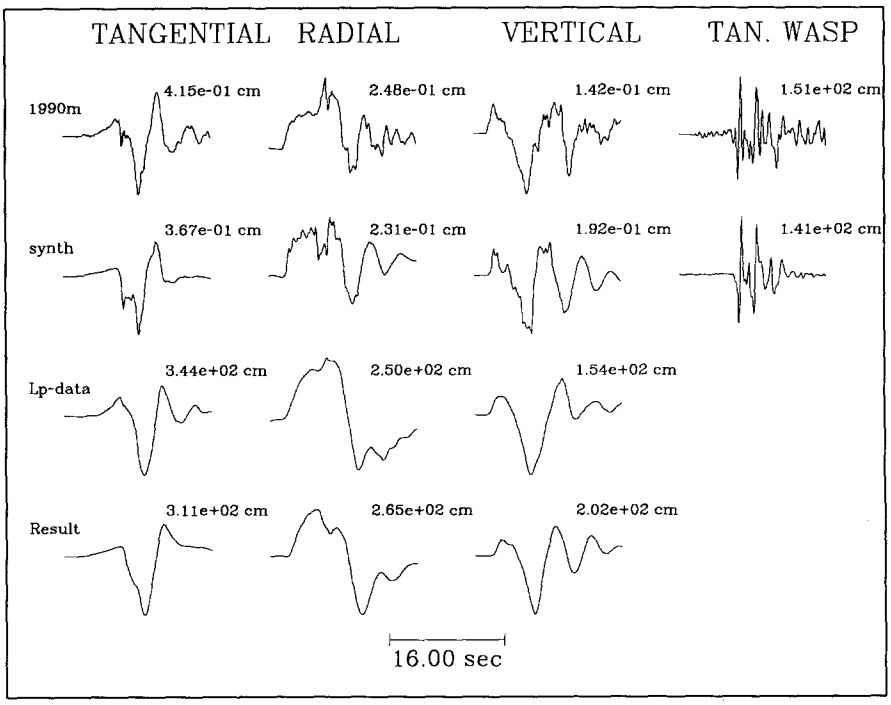

FIG. 6. Long-period inversion using the sum.lag1 Green's functions. 1990m is the 1990 main shock displacement and tangential WASP waveform data. "synth" is the predicted displacements and tangential WASP computed with a mechanism determined by inverting the long-period data using the sum.lag1 Green's functions. "Lp-data" is the simulated Press-Ewing data as in Figure 4a. "Result" is the Press-Ewing synthetic determined by the inversion. The inversion results are: $\theta = 215°$, $\lambda = 6°$, $\delta = 74°$, and $M_0 = 2.5 \times 10^{24}$ dyne-cm. The amplitudes are in centimeters.

DISTRIBUTED FAULT MODELS

The point-source models just discussed are useful in that they accurately model the three-component displacement and tangential WASP waveforms. The best double point-source model uses a time lag of 0.50 sec between the shallow and deep sources. Next we would like to determine if such a lag time between the shallow and deep sources is physically possible given the orientation of the fault and a reasonable rupture velocity. We investigate the dimensions of the distributed fault and attempt to constrain the size of the deep asperity using the distributed finite fault summation technique after Hartzell (1978) and Heaton and Helmberger (1979). This method operates on the premise that distributed fault slip can be approximated by a summation of small subfault slips (point sources convolved with the rise time of a subfault). Using relationship (2) and assuming that each subfault source fills the interstitial spaces in the grid yet minimizing overlap, we assume $a = w/\sqrt{2}$ where w is the length of a subfault side. We use a grid spacing of 0.25 km, and a triangular time function with a duration (τ) of 0.14 sec is convolved with the subfault Green's functions. Because the distance between the fault and PAS is large compared to the length of the fault, it is assumed that the changes in the azimuth from each element on the fault to the station are small. All of the distributed fault models shown here use the orientation of the fault-plane solution and the moment obtained from the inversion of the long-period waves in which the double

point-source Green's functions were used. A rupture velocity of 3.0 km/sec (85 per cent of the shear-wave velocity in model LOHS1) is assumed. We use the locations of aftershocks (Figs. 2a and b) to obtain the initial dimension of the distributed fault and the location of the hypocenter. Figure 2a shows that the hypocenter is centered laterally in the aftershock zone, and Figure 2b shows that it is located near the top of the fault in depth. Based on these observations, we use a laterally centered hypocenter located at a depth of 6 km. The top of the fault is also located at 6 km depth. Slip complexity on the fault is accomplished by differentially weighting each of the subfaults. These subfault weights are determined in a forward modeling sense.

Figure 7 shows the results of the distributed fault modeling. The top row displays the three-component displacement and tangential WASP data as in Figure 5. The first model (uniform1) was computed using a 5 by 7 km (length by width) fault. The moment and fault plane solution obtained in the last section was used, and all of the subfault weights are equal to describe uniform slip. This model does a poor job in fitting the displacement and WASP data. Furthermore, the moment of 2.5×10^{24} dyne-cm is not large enough to produce the amplitudes observed in the data. The next model (uniform2) is also a uniform rupture model with a dimension of 5 by 3.5 km and does a much better job in modeling the displacement data. The maximum amplitudes are still too small, but there is good agreement in the displacement waveforms. The tangential WASP synthetics, although of shorter period than in the previous model, fail to fit the data. To increase the amplitudes and to use an area similar to that suggested by the long-period waves (less than 13 km^2), a 3.5 by 3.5 km fault (uniform3) was tried. This fault increases the amplitudes slightly and the displacement waveforms are fairly well modeled, however the phase S_0 is too long period and the tangential WASP is still not satisfactorily modeled. Other uniform fault models with smaller areas were tested and they resulted in larger amplitudes, but they show little improvement in explaining both the long-period and short-period data simultaneously. The progression from a 5 by 7 km fault to a 3.5 by 3.5 km fault, however, shows that a distributed fault model with a smaller area agrees with the earlier result obtained from the long-period waveform inversion.

One of the purposes of using the distributed fault models was to examine whether or not the time lag of 0.5 sec found earlier is physically possible using a reasonable rupture velocity. Much of the area southwest of the hypocenter (the area between the epicenter and B′ on Fig. 2b) has lag times less than 0.6 sec when a rupture velocity of 3 km/sec is used. The following three models use the fault area of model uniform3 and asperities containing 30 per cent of the total moment are centered 0.875 km southwest of the hypocenter at a depth of 8.5 km. The first model, asperity1, uses an asperity with an area of 0.25 km^2. This model produces arrivals that are too short period, but the synthetic WASP waveform is in good agreement with the data. The model asperity2, uses an asperity with an area of 1.0 km^2. This model produces a reasonably good fit to both the displacement and WASP data. The shape of direct P on the radial and vertical components compares well with the data, in that the seismogram begins with a gentle slope and later steepens. The tangential WASP synthetic and data are in good agreement, but there is a problem with the ratio of WASP to displacement maximum amplitudes where the synthetic value is too large. Reducing the moment of the asperity would correct this ratio. The next model

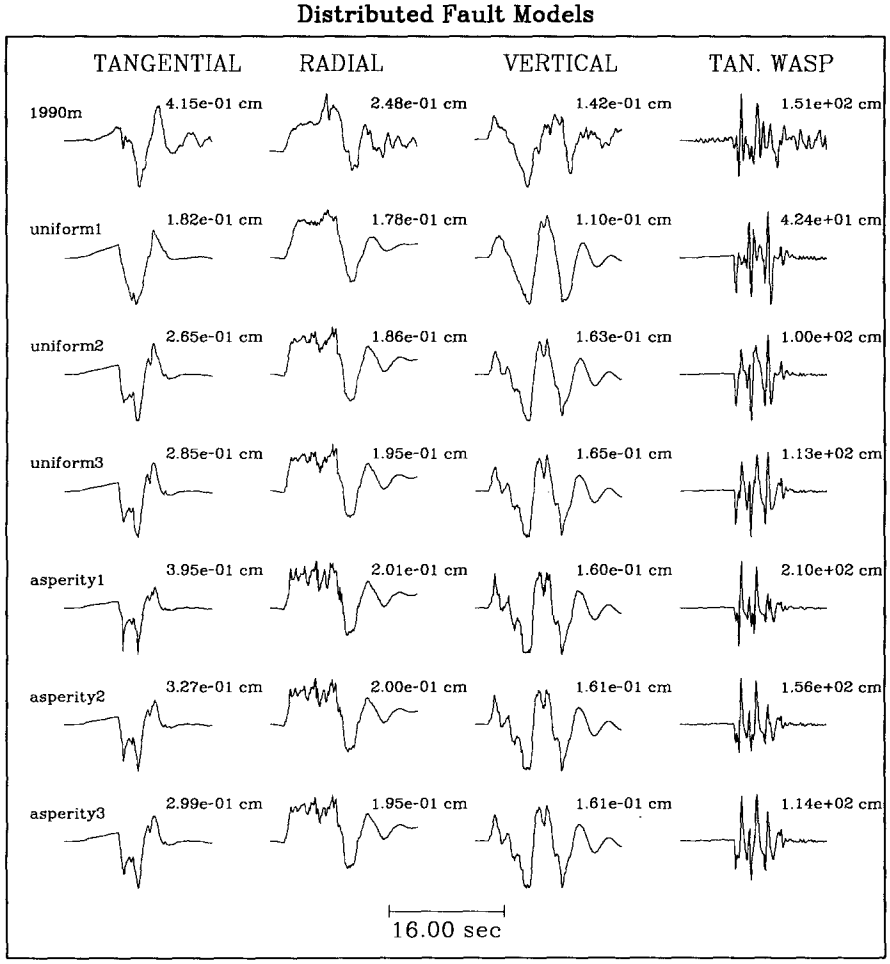

FIG. 7. Three-component displacement and tangential component WASP data for the 28 February 1990 main shock, and distributed finite fault synthetics. The moment and fault plane solution determined by using sum.lag1 Green's functions (Fig. 6) was used. Profile BB′ (Fig. 2a) shows the orientation of the finite fault relative to the aftershock zone. The hypocenter is centered laterally and located at the top of the fault at a depth of 6 km. 1990m is the displacement and tangential WASP data. "uniform1" is a uniform slip model with fault dimensions of 5 by 7 km (length by width). "uniform2" is a uniform slip model with fault dimensions of 5 by 3.5 km (length by width). "uniform3" is a uniform slip model with fault dimensions of 3.5 by 3.5 km (length by width). "asperity1" is a distributed slip model with a 0.25 km^2 asperity releasing 30 per cent of the total moment. The center of the asperity is located at 0.875 km southwest of the hypocenter at a depth of 8.5 km. "asperity2" is a distributed slip model with a 1.0 km^2 asperity releasing 30 per cent of the total moment. The center of the asperity is in the same location as model "asperity1." "asperity3" is a distributed slip model with a 2.25 km^2 asperity releasing 30 per cent of the total moment. The center of the asperity is in the same location as model "asperity1." The amplitudes are in centimeters.

(asperity3) uses an asperity with an area of 2.25 km^2. This model produces good waveform fits to both the displacement and WASP data, however the tangential and radial amplitudes are lower than in the data. There is some broadening of S_0 in both the displacement and WASP synthetics, and this model probably represents an upper bound for the size of the asperity.

The relatively low amplitudes in the distributed fault models could be due to directivity that we did not consider. All of our calculations assume bilateral

rupture horizontally. To better understand lateral directivity, it would be necessary to use multiple stations with good azimuthal coverage, and of course Green's functions for the paths to these stations that accurately model the source depth dependence in the data. In addition, the amplitudes would increase if the main shock ruptured an area smaller than used in model uniform3 with an asperity located on the periphery or beyond the region of the main shock slip. Furthermore, small changes in fault orientation could affect the amplitudes and waveforms of the short periods while having little affect on the long periods. Additional complexities that we did not consider and would not be able to resolve with single station data are multiple slips, variable rupture velocity, complicated subfault time functions, and any combination of these. The number of parameters in the simplified distributed finite fault model we use and the levels of complexity neglected make this problem tremendously nonunique. While these distributed fault models do not produce synthetics that fit better than the double point-source models, they do lend support for the small faulting area suggested by the long-period data and the timing of the second point-source in model sum.lag1.

Discussion and Conclusions

The availability of Green's functions for the path from Upland to Pasadena, California, provided an opportunity to invert the long-period, three-component waveform data recorded at PAS for source information. The long-period source of the 1990 Upland main shock had a strike (θ) of 216°, rake (λ) of 5°, dip (δ) of 77°, moment of 2.5×10^{24} dyne-cm, and a duration (τ) of 1.2 sec. The depth was relatively shallow at about 6 km. The above fault-plane solution and source depth are in good agreement with the results of Hauksson and Jones (1991). This result is important in that it demonstrates the power of using three-component, broadband, high-dynamic range data in source studies of large historic and future earthquakes where smaller, simpler events are available to determine crustal Green's functions to calibrate various paths.

The epicenters of the three events discussed in this article plot on the inferred trace of the Cucamonga fault. In this area, the Cucamonga fault bends to the south with a strike of about 225° from north, which is consistent with the four focal mechanisms in Table 2 and the mechanism determined in this article. The dip of surface exposures located east of the Upland source region on the Cucamonga fault are about 35° to the north (Cramer and Harrington, 1987). The primary problems with the Cucamonga fault being the causative structure is that the observed dip of the aftershocks (Fig. 2a) and the dips of the fault plane solutions are much steeper. Furthermore, Hauksson and Jones (1991) point out that the aftershock zone lies southeast of the inferred trace of the Cucamonga fault and projects to the location of the San Jose fault. It must be noted, however, that the location of the Cucamonga fault in this area is inferred, and concealed by alluvial deposits. It is possible the pronounced change in strike mentioned above is accompanied by a steepening of dip.

The San Jose fault to the east of the epicentral location (Fig. 2a) is a likely candidate as the causative structure. The southern extension of the San Jose fault within the San Jose Hills shows left-lateral offset (Cramer and Harrington, 1987). The location of the northern portion of the San Jose fault is inferred from basement topography in which the southeast side is faulted down relative to the northwest side (Yerkes *et al.*, 1965; Jennings, 1975) and from ground

water barriers (California Dept. Water Res., 1970). Our fault-plane solution is consistent with the vertical sense of motion on the fault in that it shows a slight thrust component in which the northwest side is up relative to the southeast side. The thrust component is small, however, and the motion is predominantly left-lateral strike-slip. The Upland earthquakes occurred in a complicated region in which there are several inferred faults in close proximity, and unfortunately there are no surface exposures of the event to confirm the sense of slip on the fault. It is possible that the apparent vertical offset across the San Jose fault could be due to strike-slip faulting of an irregular surface.

Both the point-source and distributed fault models require a complicated rupture that includes an asperity at 8 to 9 km depth. The ratio of tangential displacement amplitude to tangential WASP amplitude constrain the size of the asperity to be about 30 per cent of the total moment. Assuming a circular fault for the asperity stress drop is defined as $\Delta\sigma = 7M_0/16a^3$ (Kanamori and Anderson, 1975), where $\Delta\sigma$ is the stress drop in dyne-cm^{-2}, M_0 is the seismic moment, and a is the fault radius as defined in equation (2). The models sum.lag1, asperity1, and asperity2 have greater than 1 kbar stress drops for the asperity. The long-period stress drop is 265 bars. The distributed fault models with uniform slip also indicate that the fault area was smaller than the aftershock zone. Using a rupture velocity of 3.0 km/sec and the long-period fault orientation, it is possible to have a lag of 0.5 sec for an asperity located at 8 to 9 km depth, as suggested by the double point-source modeling. Similar results were also obtained using a rupture velocity of 2.8 km/sec.

It is interesting to compare the aftershock distribution with depth (Fig. 2b) with the location of the asperity and the long-period source area determined by the inversion. Figure 2b shows that at 9 km depth there is a change in the dip of the fault. Below 9 km depth there are two trends, one continuing with a steep dip and the other with a shallower dip. The shallow dip lies north of the line AA′ and the steeper dip lies to the south of AA′ (Hauksson and Jones, 1991). The changes in dip of the fault at this depth could be a source of stress accumulation, as evidenced by the large stress drop of the asperity. Additional evidence is a clustering of the larger aftershocks at this depth. Furthermore, the best-fitting long-period point-source solution gives a source duration of 1.2 sec, which according to equation (2) corresponds to an 8-km^2 fault. This is a factor of 5 smaller than the area of the aftershock zone. The distributed fault models with uniform slip also indicate that the fault area was smaller than the aftershock zone. Thus our modeling results argue that the main shock did not rupture deeper than 9 km depth. It is possible that the observed fault complexity at this depth inhibited the propagation of the main shock rupture front.

There is also a rather abrupt termination of aftershocks above 4 km depth. The velocity model LOHS1 from which we calculated our synthetics has an interface at this depth in which there is about a 25 per cent reduction in *S*-wave velocity. In comparison, the more regional velocity model SoCal (Table 1), used to locate the events and to determine fault-plane solutions, has its shallowest interface at 5.5 km. Artifacts introduced into the locations of the hypocenters would occur at the depth of this interface and not shallower as observed (Hauksson and Jones, 1991). Thus, abrupt termination of aftershocks at about 4 km depth could represent a change in material properties, perhaps caused by a lack of strength.

In conclusion, the use of broadband waveform data compliments first-motion

studies by providing additional constraints to focal depth and focal mechanism determinations as demonstrated in this study. With the continued installation of broadband stations, effort needs to be directed at developing Green's functions from potential source regions to these stations. Such a calibrated network will have the potential for quick assessment of strong earthquakes, as well as providing the detailed information needed to better understand source physics.

ACKNOWLEDGMENTS

The authors acknowledge Chandan Saikia for his efforts in developing the F-K code used in this study. We thank David Boore, Robert Graves, Egill Hauksson, and Bradley Woods for their meaningful reviews. We benefited from discussions with Hiroo Kanamori regarding the Pasadena broadband, high-dynamic range instrument and data processing codes he made available. This research was supported by the National Science Foundation grant EAR9014787. Contribution No. 4910, Division of Geological and Planetary Sciences, California Institute of Technology, Pasadena, California.

REFERENCES

Brune, J. N. (1970). Tectonic stress and the spectra of seismic shear waves from earthquakes, *J. Geophys. Res.* **75**, 4997-5009.

California Dept. Water Res. (1970). Meeting water demands in the Chino-Riverside Area: Appendix A—Water Supply, *Calif. Dept. Water Res. Bull* **104-3**, 108 pp.

Cohn, S. N., T. Hong, and D. V. Helmberger (1982). The Oroville earthquakes: a study of source characteristics and site effects, *J. Geophys. Res.* **87**, 4585-4594.

Cramer, C. H. and J. M. Harrington (1987). Seismicity and tectonics of the Cucamonga fault and the eastern San Gabriel mountains, San Bernardino County, *U.S. Geol. Surv. Profess. Pap. 1339*, 7-26.

Dreger, D. S. and D. V. Helmberger (1990). Broadband modeling of local earthquakes, *Bull. Seism. Soc. Am.* **80**, 1162-1179.

Hartzell, S (1978). Earthquake aftershocks as Green's functions, *Geophys. Res. Lett.* **5**, 1-5.

Hauksson, E. and L. M. Jones (1991). The 1988 and 1990 Upland earthquakes: left-lateral faulting adjacent to the central Transverse Ranges, Transverse Ranges, *J. Geophys. Res.* **96**, 8143-8165.

Heaton, T. H. and D. V. Helmberger (1979). Generalized ray models of the San Fernando earthquake, *Bull. Seism. Soc. Am.* **69**, 1311-1341.

Helmberger, D. V. and S. D. Malone (1975). Modeling local earthquakes as shear dislocations in a layered half space, *J. Geophys. Res.* **80**, 4881-4888.

Jennings, C. W. (1975). Fault map of California with locations of volcanoes, thermal springs and thermal wells, California Division of Mines and Geology, No. 1.

Kanamori, H. and D. L. Anderson (1975). Theoretical basis of some empirical relations in seismology, *Bull. Seism. Soc. Am.* **65**, 1073-1095.

Kanamori, H., J. Mori, and T. H. Heaton (1990). The 3 December 1988, Pasadena earthquake (M_L = 4.9) recorded with the very broadband system in Pasadena, *Bull. Seism. Soc. Am* **80**, 483-487.

Liu, H. and D. V. Helmberger (1985). The 23:19 Aftershock of the 15 October 1979 Imperial Valley earthquake: more evidence for an asperity, *Bull. Seism. Soc. Am.* **75**, 689-708.

Mori, J. and S. Hartzell (1990). Source inversion of the 1988 Upland earthquake: determination of a fault plane for a small event, *Bull. Seism. Soc. Am.* **80**, 507-518.

Yerkes, R. F., T. H. McCulloh, J. E. Schoellhamer, and J. G. Vedder (1965). Geology of the Los Angeles Basin California: an introduction, *U.S. Geol. Surv. Profess. Pap. 420-A*, 57 pp.

SEISMOLOGY LABORATORY
CALIFORNIA INSTITUTE OF TECHNOLOGY 252-21
PASADENA, CALIFORNIA 91125

Manuscript received 20 August 1990